2438 Vol. 47, No. 10 / 15 May 2022 / Optics Letters Letter

Optics Letters

Quartic Kerr cavity combs: bright and dark solitons

Pedro Parra-Rivas,[1,2,5] Sabrina Hetzel,[3] Yaroslav V. Kartashov,[4] Pedro Fernández de Córdoba,[1] J. Alberto Conejero,[1] Alejandro Aceves,[3] and Carles Milián[1,6]

[1] Institut Universitari de Matemàtica Pura i Aplicada, Universitat Politècnica de València, 46022 València, Spain
[2] Dipartimento di Ingegneria dell'Informazione, Elettronica e Telecomunicazioni, Sapienza Universitá di Roma, Via Eudossiana 18, 00184 Rome, Italy
[3] Department of Mathematics, Southern Methodist University, Dallas, Texas 75275, USA
[4] Institute of Spectroscopy, Russian Academy of Sciences, Troitsk, Moscow 108840, Russia
[5] e-mail: pedro.parra-rivas@uiniroma1.it
[6] e-mail: carmien@upvnet.upv.es

Received 14 February 2022; revised 30 March 2022; accepted 30 March 2022; posted 31 March 2022; published 3 May 2022

We theoretically investigate the dynamics, bifurcation structure, and stability of localized states in Kerr cavities driven at the pure fourth-order dispersion point. Both the normal and anomalous group velocity dispersion regimes are analyzed, highlighting the main differences from the standard second-order dispersion case. In the anomalous regime, single and multi-peak localized states exist and are stable over a much wider region of the parameter space. In the normal dispersion regime, stable narrow bright solitons exist. Some of our findings can be understood using a new, to the best of our knowledge, scenario reported here for the spatial eigenvalues, which imposes oscillatory tails to all localized states.

https://doi.org/10.1364/OL.455944

The possibility of exciting robust temporal solitons in fiber loops [1] and microring resonators [2,3] has a profound impact on the fundamentals and applications of frequency combs [4,5]. A clear advantage of driven systems with respect to single-pass ones is the fact that ultra-short solitonic pulses exist and are robust under strong perturbations arising due to the so-called higher-order effects, both of linear [6–8] and nonlinear [9–11] nature, as well as in higher dimensions [12,13]. Not surprisingly, dispersion engineering was shown to be a versatile tool for the control of many morphological properties of solitonic combs, such as the enhancement of their spectral extent [14,15]. In this respect, generalizations of Schrödinger solitons to waveguides with dominant quartic dispersion—pure quartic solitons (PQSs) [16,17]—are attractive because of their flatter spectra and favorable energy scaling with pulse duration, as demonstrated with mode-locked lasers [18] and predicted also for microring resonators [19]. These properties make them potentially important to increase the power of ultra-short solitons from high-Q microrings. PQSs in microrings were predicted in Ref. [20] and shown to be robust under Raman scattering [21].

In this Letter, we report on the bifurcation structure of PQSs in Kerr cavities with normal and anomalous group velocity dispersion (GVD). When GVD is anomalous, single and multi-peak bright localized states (LSs; dissipative solitons), are found to coexist over the entire parameter space, and to remain robust over a much larger area of the parameter region than in the second-order dispersion system described by the Lugiato–Lefever equation (LLE) [22]. With normal GVD, stable dark and bright solitons (BSs) exist. The latter refer to the widest dark solitons and, in contrast to the LLE, are stable over a finite interval of parameters. BSs can be predicted by dynamical system theory, which ubiquitously imposes oscillatory tails to all PQSs.

Under a dominant fourth-order dispersion (FOD), the time evolution of the intra-cavity field envelope, A, may be described by the pure quartic Lugiato–Lefever (PQLL) equation:

$$\partial_t A = -(1 + i\Delta)A - i\omega_4\partial_x^4 A + iA|A|^2 + S. \qquad \textbf{(1)}$$

Here, the periodic coordinate, x, is related to the physical length, X, by $x = X\sqrt{\gamma}/[2\pi R\sqrt{|B_4|}]$, where R is the cavity radius, γ is the normalized loss, and B_4 is the FOD coefficient.

The spectral combs in this work are shown as a function of the wavenumber $k = (m - m_0)/R$, where m_0 is the cavity mode excited by S (see, e.g., Ref. [13] for scaling). In Eq. (1), ω_4 takes the value $+1$ (-1) to account for parabolic anomalous (normal) GVD. We note that such seemingly idealized GVD landscapes are, in fact, attainable with $\omega_4 = \pm 1$ around the telecom band with fibers [23,24] and microrings [25]. Residual second- and third-order dispersion are not expected to play a significant role, as long as the GVD sign remains constant. Equation (1) is integrated in time using the fourth-order Runge–Kutta method, while stationary states and their stability are computed using the Newton–Raphson method and the corresponding Jacobian.

We first focus on the anomalous GVD case ($\omega_4 = 1$). The energy, defined as the L_2-norm $||A||^2 = l^{-1}\int_{-l/2}^{l/2}|A(x)|^2dx$ (with $l = 2\pi R$), of the homogeneous steady state (HSS) A_h, is shown in Figs. 1(a) and 1(b) using solid (dashed) lines for stable (unstable) states (green curves). For these parameters, the HSS undergoes a pair of saddle-node (SN) bifurcations that we label $\mathrm{SN}_h^{l,r}$. For norms above SN_h^r, many unstable families of pure quartic Turing (periodic) patterns bifurcate sub-critically from the branching point (BP) on the HSS. Examples of such branches are plotted in Figs. 1(a) and 1(b) (red curve) and as enlarged views in

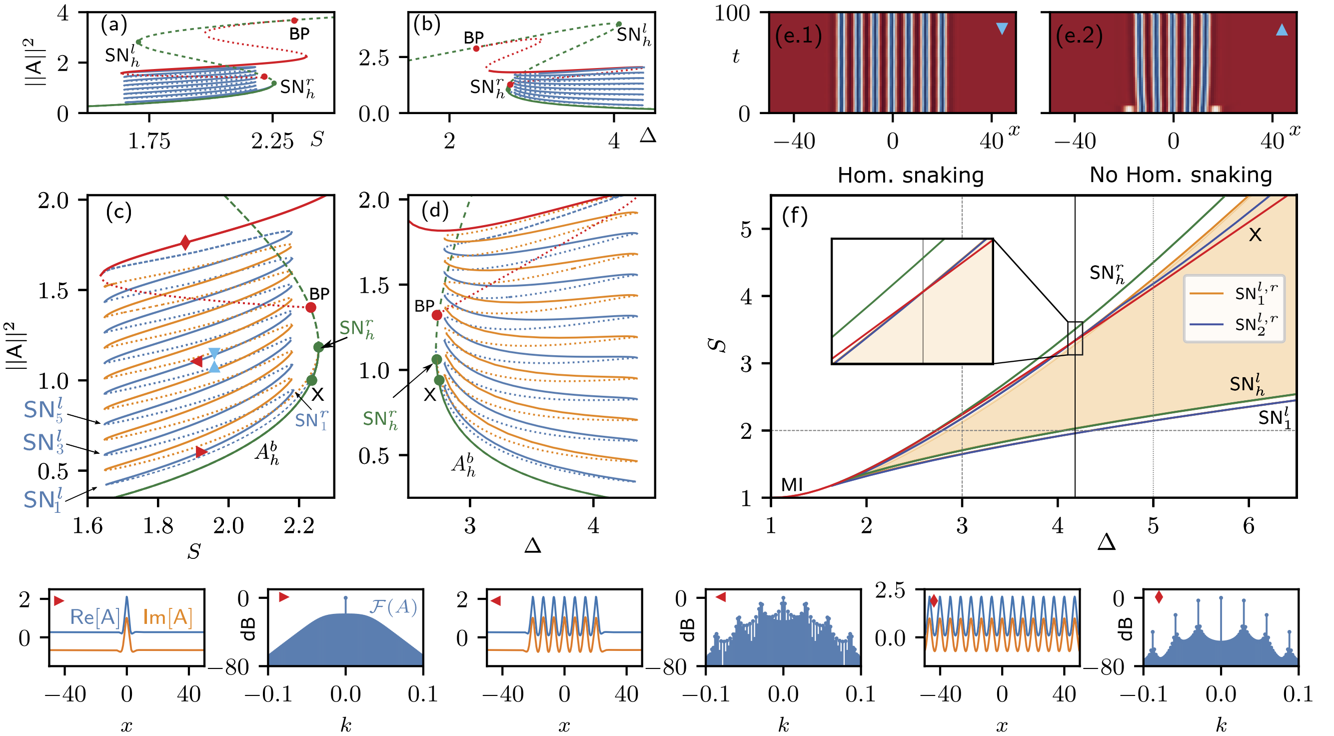

Fig. 1. (a)–(d) Norm branches for the HSS (green), LSs (blue, orange), and a pattern family (red) for $\omega_4 = 1$ and (a), (c) $\Delta = 3$, (b), (d) $S = 2$; (c), (d) enlargement around the snaking curves in (a), (b). Solid (dashed) lines denote stability (instability), and red symbols correspond to the states shown in the insets. (e) Evolution of (e.1) stable and (e.2) unstable multi-peak LSs. (f) Phase diagram in (Δ, S)-parameter space, showing main bifurcation lines. Straight dashed gray lines at $S = 2$, $\Delta = 3$, and $\Delta = 5$ mark, respectively, the phase space locations of the data shown in (b), (d), (a), (c), and Fig. 2. The inset in panel (f) shows the crossing (see vertical line) between the Belyakov–Devaney–analog (red) transition and SN_2^r (blue), marked by the vertical solid line.

Figs. 1(c) and 1(d). An example of one such pattern is shown in the panels in Fig. 1 marked with a lozenge, in spatial and Fourier domains. Because patterns and HSSs, both stable, coexist over a finite interval in pump amplitude, S, [Figs. 1(a) and 1(c)] or detuning, Δ [Figs. 1(b) and 1(d)], LSs consisting of a slug of the pattern embedded in a HSS (i.e., partly pattern, partly flat state) may form, owing to the locking of fronts [26]. The norm of LSs is shown in Figs. 1(c) and 1(d) by blue (orange) curves corresponding to LSs with an odd (even) number of peaks. Examples of LSs are represented in the panels in Fig. 1 marked with a left-pointing or right-pointing arrowhead. LS branches at higher values of $||A||^2$ correspond to spatially wider states because two pattern peaks nucleate symmetrically on each side of the LSs when branches fold back toward smaller pump values (larger detuning) across the saddle-nodes depicted in Figs. 1(c) and 1(d). This back-and-forth snaking of the LS branches corresponds to standard homoclinic snaking [26]. The evolution of a stable and unstable multi-peak state is shown in Figs. 1(e.1) and 1(e.2), respectively.

Figure 1(f) depicts relevant bifurcations in (Δ, S)-parameter space and shows the existence domain of LSs (shaded area). The lower HSS state, A_h^b, becomes unstable for values of S above the red line (for which $I_h \equiv ||A_h||^2 = 1$), which corresponds to modulational instability (MI) when $\Delta<2$.

In the Lugiato–Lefever (LL) system, the homoclinic snaking shown in Fig. 1 ceases to exist for $\Delta \geq 2$ because (for $\Delta = 2$) the rightmost [leftmost] saddle-nodes of the LSs, SN_i^r, shown in Figs. 1(c) [1(d)], collide with a homoclinic bifurcation occurring at a Belyakov–Devaney transition (marked X) [27]. As a result,

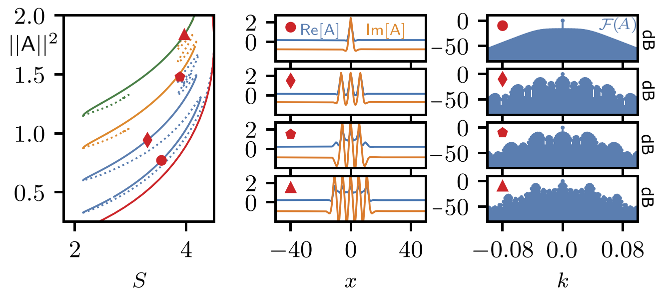

Fig. 2. (left column) Disconnected standard homoclinic snaking branches for LS families with an odd number of peaks and $\Delta = 5$, (center column) selected LS profiles, and (right column) associated frequency spectra.

single-peak BSs connect with spatially equispaced multi-peak LSs, forming a *foliated snaking* [28,29]. On the contrary, in the PQLL system, the SN_i^r collides with the point X at a larger detuning, $\Delta \approx 4.15$ [cf. Fig. 1(f)], thus considerably broadening the region where standard homoclinic snaking occurs. Above $\Delta \approx 4.15$, the homoclinic snaking breaks up, yielding bifurcation curves of the type shown in Fig. 2 for $\Delta = 5$, which do not seem to *connect* all LSs with odd (nor with even) numbers of peaks. Interestingly, in this high detuning region ($\Delta>4.15$), LSs still exist (cf. Fig. 2). The much larger region of the phase space in which LSs exist in the PQLL system provides a unique scenario to observe these solitary waves.

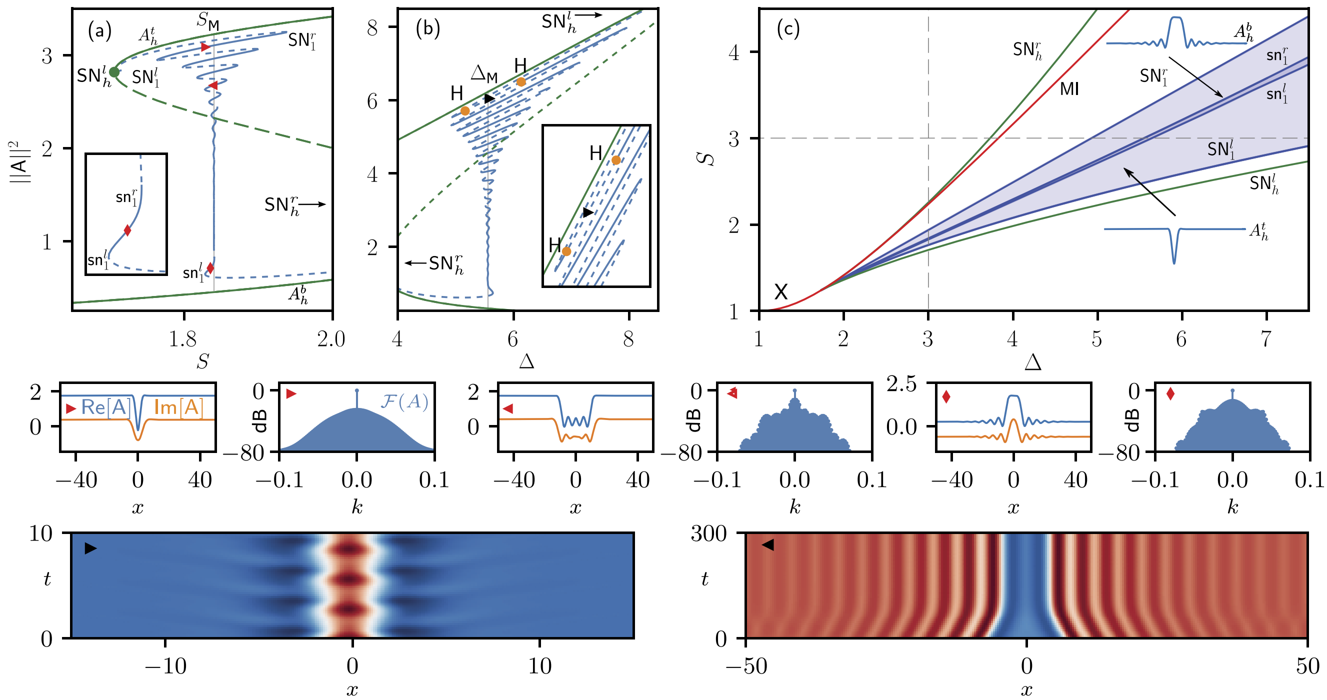

Fig. 3. Collapsed homoclinic snaking (blue) for $\omega_4 = -1$ and (a) $\Delta = 3$, (b) $S = 3$. The multi-valued HSS is also shown (green). Solid (dashed) lines correspond to stable (unstable) states. Red symbols in (a) correspond to the LSs shown in the insets. H labels in (b) mark Hopf bifurcations. (c) Phase diagram on the (Δ, S)-plane showing the main bifurcations of the system. Bottom insets show excitation of (left) unstable dark and (right) stable bright states (see markers for reference).

We now turn to the normal GVD case ($\omega_4 = -1$). Because the HSSs and corresponding stability thresholds are identical to those of the LLE, the system presents two uniform states that coexist and are stable: the bottom (A_h^b) and top (A_h^t) branches. In this situation, plane fronts, domain walls, or switching waves (SWs) may form, interact, and bind together, leading to the formation of LSs. Our findings are summarized in Fig. 3. Similarly to the LL system, dark solitons bifurcate from SN_h^l and undergo collapsed homoclinic snaking [30]: an oscillatory bifurcation curve that damps to the uniform Maxwell point (S_M or Δ_M) of the system as $||A||^2$ decreases [cf. Figs. 3(a) and 3(b)]. Selected LSs are shown in the panels in Fig. 3 marked with a red left-pointing or right-pointing arrowhead. LSs existing between two saddle-node bifurcations often present Hopf instability [cf. Fig. 3(b)], leading to the appearance of breathers (cf. the panel in Fig. 3 marked with a black right-pointing arrowhead).

The collapsed snaking in Figs. 3(a) and 3(b) is, thus far, qualitatively identical to that of the LL system [31–33]. However, the most evident and interesting distinctive feature here is the presence of a stable branch at the bottom of the diagram, shown in close-up view in Fig. 3(a), limited by $sn_1^{l,r}$, which does not exist in the LLE. The LSs along this branch are stable BSs, similar to those found under other higher-order effects [10,33–35] and reminiscent of the narrowest platicons found in [31] (cf. the panels in Fig. 3 marked with a lozenge). Figure 3(c) shows reference bifurcations on the (Δ, S) plane. HSS bistability exists between SN_h^l and SN_h^r (see green curves), A_h^b exhibits MI in the region between the red curve and SN_h^r. The narrowest and stable dark LSs exist within the light shaded region (limited by $SN_1^{r,l}$) and BSs are found within the narrowest shaded region (between sn_1^l and sn_1^r).

The origin of these narrow BSs can be formally understood by means of dynamical system theory [36]. Briefly, defining $U = \mathrm{Re}[A(x)]$, $V = \mathrm{Im}[A(x)]$, and $y(x) = [U, U', U'', U''', V, V', V'', V''']^{\mathrm{T}}$, it is possible to cast Eq. (1) in the form $y'(x) = f(y(x); \Delta, S, \omega_4)$, which, linearized around a HSS y_0, reads $y'(x) = \mathcal{J}(y_0)y(x) + O(y^2(x))$. The eigenvalues, λ, of the Jacobian matrix $\mathcal{J}(y_0)$ determine whether the tails of a stationary state (SWs or otherwise) are oscillatory ($\mathrm{Im}[\lambda] \neq 0$) or monotonic ($\mathrm{Im}[\lambda] = 0$) and solve the bi-quartic equation

$$\lambda^8 - (4I_h - 2\Delta)\omega_4\lambda^4 + 3I_h^2 - 4\Delta I_h + \Delta^2 + 1 = 0. \quad \textbf{(2)}$$

This equation transforms into that corresponding to the LLE by substituting $\lambda \to \pm\sqrt{i\lambda_{\mathrm{LL}}}$ and $\omega_4 \to \omega_2$ (ω_2 is the GVD coefficient). With this simple connection between the LL and the PQLL systems (and taking into account that the HSSs are exactly the same in both cases), it is straightforward to relate the eigenvalue distributions of both in a general way.

In the LLE, four different types of eigenvalue distribution, corresponding to saddle (S), saddle-focus (SF), double center (DC), and saddle-center (SC) fixed points, are known [37] (open circles in Fig. 4). The relation $\lambda \to \pm\sqrt{i\lambda_{\mathrm{LL}}}$ allows us to visualize the eigenvalue distributions of the PQLL (see filled circles in Fig. 4).

SWs connect the bottom and top HSSs ($A_h^{b,t}$), which in the LLE are always an SF and an S, respectively [32]. Hence, oscillations only exist in the lower state of the SW. In that case, short dark LSs form easily, while short bright LSs (or, equivalently, extremely long dark LSs) struggle to form. On the contrary, in the PQLL, the saddle (S) fixed point becomes a quatri-focus (top-right panel in Fig. 4) with nonzero $\mathrm{Im}\{\lambda\}$. This induces oscillations on the top HSS, A_h^t, and BSs appear, owing to the locking of plane fronts

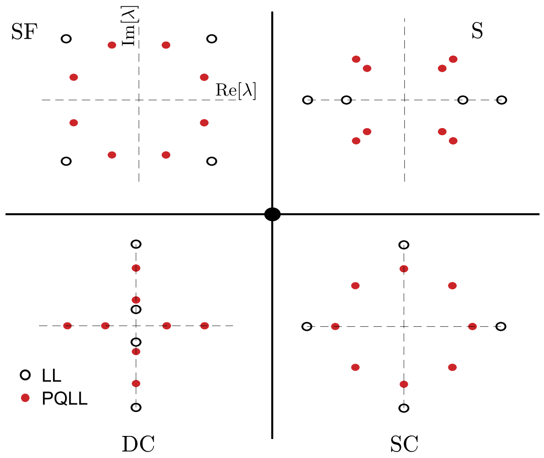

Fig. 4. General picture of spatial eigenvalue distributions for standard LL (open circles) and PQLL [Eq. (1)] (filled circles) equations.

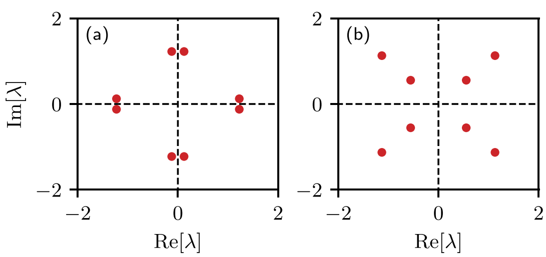

Fig. 5. Spatial eigenvalues associated with the BS in the panels in Fig. 3 marked with a lozenge are shown for: (a) the bottom state A_h^b with $(\omega_4, \Delta, I_h) = (-1, 3, 0.44)$; (b) the top state A_h^t with $(\omega_4, \Delta, I_h) = (-1, 3, 3.22)$.

around such states. In particular, the set of spatial eigenvalues shown in Figs. 5(a) and 5(b) correspond to the lower and upper states of the SWs that bind together to form the BS in the panels in Fig. 3 marked with a lozenge. The process of interaction of two SWs around A_h^t and the locking into a BS is evident from the panel in Fig. 3 marked with a left-pointing arrowhead.

To conclude, we presented the bifurcation structure, existence, and stability of LSs in the PQLL system with normal and anomalous GVD. In the anomalous case, LSs exist as stable states over a much larger region than in the LL system. In the normal GVD regime, stable BSs exist, owing to SW locking over their tops. Some of the qualitative differences found here with respect to the LLE can be formally understood using dynamical system theory.

Funding. National Science Foundation, Division of Mathematical Sciences (1909559, 1840260); Research Executive Agency (101023717).

Acknowledgment. PPR acknowledges the European Union's Marie Sklodowska-Curie grant 101023717. SH and AA have been supported by NSF RTG grant DMS-1840260 and AA was supported by grant NSF/DMS-1909559. SH and AA also benefited from discussions with Dr. Ross Parker. YVK and CM gratefully acknowledge discussions with Professor L. Torner.

Disclosures. The authors declare no conflicts of interest.

Data availability. Data underlying the results in this paper may be obtained from the authors upon reasonable request.

REFERENCES

1. F. Leo, S. Coen, P. Kockaert, S.-P. Gorza, P. Emplit, and M. Haelterman, Nat. Photonics **4**, 471 (2010).
2. T. Herr, V. Brasch, J. D. Jost, C. Y. Wang, N. M. Kondratiev, M. L. Gorodetsky, and T. J. Kippenberg, Nat. Photonics **8**, 145 (2014).
3. X. Xue, Y. Xuan, Y. Liu, P.-H. Wang, S. Chen, J. Wang, D. E. Leaird, M. Qi, and A. M. Weiner, Nat. Photonics **9**, 594 (2015).
4. A. Pasquazi, M. Peccianti, L. Razzari, D. J. Moss, S. Coen, M. Erkintalo, Y. K. Chembo, T. Hansson, S. Wabnitz, P. Del'Haye, X. Xue, A. M. Weiner, and R. Morandotti, Phys. Rep. **729**, 1 (2018).
5. T. J. Kippenberg, R. Holzwarth, and S. A. Diddams, Science **332**, 555 (2011).
6. C. Milián and D. V. Skryabin, Opt. Express **22**, 3732 (2014).
7. P. Parra-Rivas, D. Gomila, F. Leo, S. Coen, and L. Gelens, Opt. Lett. **39**, 2971 (2014).
8. V. Brasch, M. Geiselmann, T. Herr, G. Lihachev, M. H. P. Pfeiffer, M. L. Gorodetsky, and T. J. Kippenberg, Science **351**, 357 (2016).
9. C. Milián, A. V. Gorbach, M. Taki, A. V. Yulin, and D. V. Skryabin, Phys. Rev. A **92**, 033851 (2015).
10. P. Parra-Rivas, S. Coulibaly, M. G. Clerc, and M. Tlidi, Phys. Rev. A **103**, 013507 (2021).
11. M. Karpov, M. H. P. Pfeiffer, H. Guo, W. Weng, J. Liu, and T. J. Kippenberg, Nat. Phys. **15**, 1071 (2019).
12. C. Milián, Y. V. Kartashov, D. V. Skryabin, and L. Torner, Phys. Rev. Lett. **121**, 103903 (2018).
13. S. B. Ivars, Y. V. Kartashov, L. Torner, J. A. Conejero, and C. Milián, Phys. Rev. Lett. **126**, 063903 (2021).
14. Y. Okawachi, M. R. E. Lamont, K. Luke, D. O. Carvalho, M. Yu, M. Lipson, and A. L. Gaeta, Opt. Lett. **39**, 3535 (2014).
15. M. H. P. Pfeiffer, C. Herkommer, J. Liu, H. Guo, M. Karpov, E. Lucas, M. Zervas, and T. J. Kippenberg, Optica **4**, 684 (2017).
16. A. Höök and M. Karlsson, Opt. Lett. **18**, 1388 (1993).
17. A. Blanco-Redondo, C. M. de Sterke, J. E. Sipe, T. F. Krauss, B. J. Eggleton, and C. Husko, Nat. Commun. **7**, 10427 (2016).
18. A. F. J. Runge, D. D. Hudson, K. K. Tam, C. M. de Sterke, and A. Blanco-Redondo, Nat. Photonics **14**, 492 (2020).
19. H. Taheri and A. B. Matsko, Opt. Lett. **44**, 3086 (2019).
20. C. Bao, H. Taheri, L. Zhang, A. Matsko, Y. Yan, P. Liao, L. Maleki, and A. E. Willner, J. Opt. Soc. Am. B **34**, 715 (2017).
21. K. Liu, S. Yao, and C. Yang, Opt. Lett. **46**, 993 (2021).
22. L. A. Lugiato and R. Lefever, Phys. Rev. Lett. **58**, 2209 (1987).
23. L. E. Hooper, P. J. Mosley, A. C. Muir, W. J. Wadsworth, and J. C. Knight, Opt. Express **19**, 4902 (2011).
24. A. M. Heidt, J. Opt. Soc. Am. B **27**, 550 (2010).
25. S. Yao, K. Liu, and C. Yang, Opt. Express **29**, 8312 (2021).
26. P. D. Woods and A. R. Champneys, Phys. D **129**, 147 (1999).
27. A. R. Champneys, Phys. D **112**, 158 (1998).
28. P. Parra-Rivas, D. Gomila, L. Gelens, and E. Knobloch, Phys. Rev. E **97**, 042204 (2018).
29. Z. Qi, S. Wang, J. Jaramillo-Villegas, M. Qi, A. M. Weiner, G. D'Aguanno, T. F. Carruthers, and C. R. Menyuk, Optica **6**, 1220 (2019).
30. J. Knobloch and T. Wagenknecht, Phys. D **206**, 82 (2005).
31. V. E. Lobanov, G. Lihachev, T. J. Kippenberg, and M. L. Gorodetsky, Opt. Express **23**, 7713 (2015).
32. P. Parra-Rivas, E. Knobloch, D. Gomila, and L. Gelens, Phys. Rev. A **93**, 063839 (2016).
33. P. Parra-Rivas, D. Gomila, and L. Gelens, Phys. Rev. A **95**, 053863 (2017).
34. Z. Li, Y. Xu, S. Coen, S. G. Murdoch, and M. Erkintalo, Optica **7**, 1195 (2020).
35. J. H. Talla Mbé, C. Milián, and Y. K. Chembo, Eur. Phys. J. D **71**, 196 (2017).
36. S. Wiggins, *Introduction to Applied Nonlinear Dynamical Systems and Chaos, Texts in Applied Mathematics*, 2nd ed. (Springer-Verlag, 2003).
37. P. Parra-Rivas, D. Gomila, L. Gelens, and E. Knobloch, Phys. Rev. E **98**, 042212 (2018).